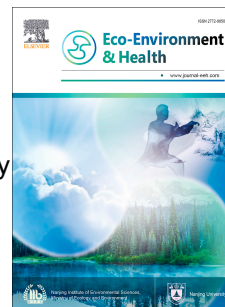


Journal Pre-proof

Effects of 3D microstructure of porous media on DNAPL migration and remediation by surface active agents in groundwater

Zhou Cheng, Ming Wu, Yanru Hao, Cehui Mo, Qusheng Li, Jianfeng Wu, Jichun Wu, Bill X. Hu, Guoping Lu



PII: S2772-9850(24)00055-3

DOI: <https://doi.org/10.1016/j.eehl.2024.08.003>

Reference: EEHL 121

To appear in: *Eco-Environment & Health*

Received Date: 19 July 2023

Revised Date: 21 July 2024

Accepted Date: 21 August 2024

Please cite this article as: Z. Cheng, M. Wu, Y. Hao, C. Mo, Q. Li, J. Wu, J. Wu, B.X. Hu, G. Lu, Effects of 3D microstructure of porous media on DNAPL migration and remediation by surface active agents in groundwater, *Eco-Environment & Health*, <https://doi.org/10.1016/j.eehl.2024.08.003>.

This is a PDF file of an article that has undergone enhancements after acceptance, such as the addition of a cover page and metadata, and formatting for readability, but it is not yet the definitive version of record. This version will undergo additional copyediting, typesetting and review before it is published in its final form, but we are providing this version to give early visibility of the article. Please note that, during the production process, errors may be discovered which could affect the content, and all legal disclaimers that apply to the journal pertain.

© 2024 The Author(s). Published by Elsevier B.V. on behalf of Nanjing Institute of Environmental Sciences, Ministry of Ecology and Environment (MEE) & Nanjing University.

1 **Effects of 3D microstructure of porous media on DNAPL migration**
2 **and remediation by surface active agents in groundwater**

3 Zhou Cheng^{a,b}, Ming Wu^{a,*}, Yanru Hao^a, Cehui Mo^a, Qusheng Li^c, Jianfeng Wu^d, Jichun
4 Wu^d, Bill X. Hu^e, Guoping Lu^a

5

6 ^aGuangdong Provincial Research Center for Environment Pollution Control and
7 Remediation Materials, College of Life Science and Technology, Jinan University,
8 Guangzhou 510632, China

9 ^bGuangdong Provincial Academy of Environmental Science, Guangzhou 510045,
10 China

11 ^cGuangdong Key Laboratory of Environmental Pollution and Health, School of
12 Environment, Jinan University, Guangzhou 510632, China

13 ^dKey Laboratory of Surficial Geochemistry, Ministry of Education; Department of
14 Hydrosciences, School of Earth Sciences and Engineering, Nanjing University,
15 Nanjing 210023, China

16 ^eSchool of Water Conservancy and Environment, University of Jinan, Jinan 250022,
17 China

18

19 *Corresponding author.

20 Email: wumingnj@foxmail.com (M. Wu)

21

22

23 **ABSTRACT**

24 Aquifers composed of porous granular media are important to human beings because
25 they are capable of storing a large amount of groundwater. Contaminant migration and
26 remediation in subsurface environments are strongly influenced by three-dimensional
27 (3D) microstructures of porous media. In this study, fractal models are developed to
28 investigate contaminant transport and surfactant-enhanced aquifer remediation (SEAR)
29 for the regular tetrahedron microstructure (RTM) and right square pyramid
30 microstructure (RSPM). The relationships of permeability and entry pressure are
31 derived for these two kinds of 3D microstructures of granular porous media. Afterward,
32 the difference in perchloroethylene (PCE) migration and SEAR efficiency between
33 RTM and RSPM is investigated by the numerical simulation based on a synthetic
34 heterogeneous granular aquifer. Results indicate that PCE penetrates faster and spreads
35 farther in RSPM-based aquifers compared with RTM-based aquifers. Further, SEAR in
36 RTM-based aquifers can achieve remediation efficiencies of 66.129%–92.214% with a
37 mean of 84.324%, which is clearly lower than the SEAR efficiency of 70.149%–94.773%
38 (with a mean of 89.122%) in RSPM-based aquifers. Findings are significant for
39 understanding the 3D microstructure of porous media and how the microstructure
40 of porous media affects macroscopic contaminant behaviors and remediation.

41 **Keywords:** Porous media; Sequential Gaussian simulation (SGS); Regular tetrahedron
42 microstructure (RTM); Right square pyramid microstructure (RSPM); Surfactant-
43 enhanced aquifer remediation (SEAR)

44

45 **1. Introduction**

46 In addition to being one of the world's most valuable freshwater resources,
47 groundwater is also a primary source of domestic drinking water for over half the
48 world's population (Boswinkel, 2000; Asuquo and Etim, 2012; Valipour, 2012;
49 Valipour, 2015; Yannopoulos et al., 2015; Valipour and Singh, 2016; Landrigan et al.,
50 2017; Demiray et al., 2023; Jeong et al., 2023; Alamooti et al., 2024; Kuang et al., 2024).

51 In recent years, however, more and more contaminants have been released into the
52 subsurface environment, especially organic contaminants released from industrial
53 emissions and leaks, such as underground storage tank spills (Bakshevskaja and
54 Pozdniakov, 2016; Cui et al., 2016; Liu et al., 2016; Landrigan et al., 2017; Wu et al.,
55 2017a; Zhang et al., 2017; Cochenec et al., 2022; Bian et al., 2023; Guo et al., 2023).
56 The issue of groundwater contamination has become a major environmental concern
57 (Liu, 2005; C.Carroll et al., 2015; Essaid et al., 2015; Huang et al., 2015; Liu et al.,
58 2016; Schaefer et al., 2016; Weathers et al., 2016; Wu et al., 2017b; Wang et al., 2023a;
59 Chen et al., 2024). The dense non-aqueous phase liquid (DNAPL) detected in
60 groundwater is toxic, carcinogenic, teratogenic, and mutagenic, posing serious
61 health risks to humans and the environment (Wang et al., 2023a; Hou et al., 2024;
62 Yang et al., 2024). When DNAPL enters the aquifer from an underground storage
63 tank, it can form residual ganglia and contaminant pools, serving as long-term
64 contamination sources (Bob et al., 2008; Liang and Lai, 2008; Liang and Hsieh, 2015;
65 Omirbekov et al., 2023; Shi et al., 2023; Herraiz-Carboné et al., 2024). Therefore,
66 groundwater restoration and subsurface environment improvement depend on the
67 investigation of DNAPL migration and remediation in aquifers.

68 Various transport characteristics are closely controlled by the microstructure of
69 materials, including hydraulic conductivity, diffusivity, and dispersivity (Yu and Li,
70 2004; Yu, 2005; Yun et al., 2005; Feng and Yu, 2007; Yun et al., 2009; Wu et al., 2017a;
71 Guo et al., 2023; Kang et al., 2023), which can strongly affect macroscopic DNAPL
72 migration and remediation in porous media. Consequently, numerous researchers
73 have examined how material microstructure affects macroscopic properties.
74 Microscale geometric structure, for instance, plays a key role in determining the
75 permeability K in Kozeny-Carman equation relating to Kozeny constant c (Bear,
76 1972; Yun et al., 2009; Shen et al., 2020). As a result of the development of fractal
77 theory, natural porous media can be viewed as fractal objects and investigated by
78 means of fractal analysis (Pfeifer and Avnir, 1983; Katz and Thompson, 1985; Krohn,
79 1988; Kim et al., 2024). For porous media, various geometrical models of
80 microstructure have been developed to study thermal conductivity, tortuosity,

81 permeability, and fluid invasion, all of which are useful for obtaining mathematical
82 models of macroscopic parameters (Yu and Cheng, 2002; Yu et al., 2009; Cai et al.,
83 2010; Yang et al., 2023). Microstructure, however, was overly idealized in previous
84 fractal models. Based on two-dimensional (2D) porous media containing spherical
85 particles, Yu and Cheng (2002) developed a simple model to quantify tortuosity and
86 permeability. A fractal method was used to derive the physical properties of porous
87 media with two phases and the invasion depth of extraneous fluids (Yu et al., 2009; Cai
88 et al., 2010; Shen et al., 2020; Yang et al., 2022). To estimate REV and investigate
89 contaminant transport in porous media, various 2D microstructure models were
90 developed by analyzing grain geometry and microarrangements of solid particles. In
91 previous studies, material microstructures were usually two-dimensional, and their
92 influence on contaminants behaviors was sparsely investigated (Yu and Cheng, 2002;
93 Yu et al., 2009; Cai et al., 2010; Wu et al., 2018, 2020, 2023).

94 The study examines the effects of microstructures on macroscopic DNAPL
95 migration and remediation using granular porous media with regular tetrahedron
96 microstructures (RTM) and right square pyramid microstructures (RSPM). In these two
97 kinds of 3D microstructures, fractal models are developed to determine permeability
98 and entry pressure mathematically. Subsequently, 200 realizations of underground
99 storage tank spill-contaminated sites are generated using a sequential Gaussian
100 simulation (SGS). Perchloroethylene (PCE) migration and remediation by surfactant-
101 enhanced aquifer remediation (SEAR) are simulated using UTCHEM. Based on
102 simulated results, the effect of microstructures on DNAPL transport and SEAR
103 efficiency is compared between RTM and RSPM.

104 **2. Methodology**

105 *2.1. Microscale fractal models of granular porous media*

106 The fractal theory suggests that porous media containing numerous pores can
107 be viewed as a bundle of capillary tubes. An infinitesimal element (unit element)
108 consisting of tortuous capillary tubes is selected from the porous media. There is a

109 relationship between the tortuous length of a capillary tube and its diameter:

$$110 \quad L_t(\lambda) = \lambda^{1-D_T} L_S^{D_T} \quad (1)$$

111 Where λ , L_t , and L_S are the diameter, the tortuous length, and the straight length of
112 the capillary tube, respectively; D_T is the fractal dimension of tortuosity.

113 Yu and Cheng (2002) found that the cumulative number of capillary tubes in a
114 unit element can be derived as follows:

$$115 \quad N(L \geq \lambda) = \left(\frac{\lambda_{max}}{\lambda}\right)^{D_f} \quad (2)$$

116 where D_f is the fractal dimension for pore/capillary areas in infinitesimal element;
117 λ_{max} is the maximum value of capillary tube diameter.

118 Afterward, the derivative of Eq. 2 can be achieved:

$$119 \quad -d_{N(L \geq \lambda)} = D_f \lambda_{max}^{D_f} \lambda^{-(D_f+1)} d\lambda \quad (3)$$

120 The total number of capillary tubes in infinitesimal element is calculated by
121 integrating Eq. 3 from λ_{min} (the minimum diameter of capillary tubes) to λ_{max} :

$$122 \quad N_t(L \geq \lambda_{min}) = \left(\frac{\lambda_{max}}{\lambda_{min}}\right)^{D_f} \quad (4)$$

123 Substituting Eq. 4 into Eq. 3 results in:

$$124 \quad -\frac{d_{N(L \geq \lambda)}}{N_t} = D_f \lambda_{min}^{D_f} \lambda^{-(D_f+1)} d\lambda = f(\lambda) d\lambda \quad (5)$$

125 where $f(\lambda) = D_f \lambda_{min}^{D_f} \lambda^{-(D_f+1)}$ is the function of probability density. If $\left(\frac{\lambda_{min}}{\lambda_{max}}\right)^{D_f} =$

$$126 \quad 0, \int_{-\infty}^{+\infty} f(\lambda) d\lambda = \int_{\lambda_{min}}^{\lambda_{max}} f(\lambda) d\lambda = 1 - \left(\frac{\lambda_{min}}{\lambda_{max}}\right)^{D_f} = 1.$$

127 Assume the flow path is L_t , and that the pressure difference between the inlet
128 and outlet is ΔP . The viscosity of fluid is μ . According to Poiseuille equation, the flow
129 rate of an individual capillary tube (q) is given by:

$$130 \quad q = \frac{\pi r^4 \Delta P}{8 \mu L} = \frac{\pi \left(\frac{\lambda}{2}\right)^4 \Delta P}{8 \mu L} = \frac{\pi \lambda^4 \Delta P}{128 \mu L} \quad (6)$$

131 The derivative of the flow rate of an individual capillary tube (q) is:

132

$$133 \quad d_q = [-d_{N(L \geq l)}] \frac{\pi \lambda^4 \Delta P}{128 \mu L}$$

$$134 \quad = \frac{\pi \Delta P}{128 \mu} \frac{D_f \lambda_{max}^{D_f}}{L_0^{D_T}} \lambda^{2+D_T-D_f} d\lambda \quad (7)$$

135 The total flow rate (Q) can be obtained by integrating q from λ_{\min} to λ_{\max} :

136 $Q = \int d\lambda$

137
$$= \int_{\lambda_{\min}}^{\lambda_{\max}} \frac{\pi}{128} \frac{\Delta P}{\mu} \frac{D_f \lambda_{\max}^{D_f}}{L_0^{D_T}} \lambda^{2+D_T-D_f} d\lambda$$

138 (8)

139
$$= \frac{\pi}{128} \frac{\Delta P}{\mu} \frac{D_f}{3+D_T-D_f} \frac{1}{L_0^{D_T}} \lambda_{\max}^{3+D_T} \left[1 - \left(\frac{\lambda_{\min}}{\lambda_{\max}} \right)^{D_f} \left(\frac{\lambda_{\min}}{\lambda_{\max}} \right)^{3+D_T-D_f} \right]$$

140

141 Due to $1 < D_T < 2$, $1 < D_f < 2$ and $3 + D_T - 2D_f > 0$, then $\left(\frac{\lambda_{\min}}{\lambda_{\max}} \right)^{D_f} \cong 0$, $0 <$
 142 $\left(\frac{\lambda_{\min}}{\lambda_{\max}} \right)^{3+D_T-D_f} < 1$. Afterward, Eq. 8 can be simplified to:

143
$$Q = \frac{\pi}{128} \frac{\Delta P}{\mu} \frac{D_f}{3+D_T-D_f} \frac{1}{L_0^{D_T}} \lambda_{\max}^{3+D_T}$$

144 (9)

144 The permeability can be derived using Darcy's law $Q = \frac{kA\Delta P}{\mu L_0}$:

145
$$k = \frac{\pi}{128} \frac{D_f}{3+D_T-D_f} \frac{L_0^{1-D_T}}{A} \lambda_{\max}^{3+D_T}$$

146 (10)

146 The tortuosity equals to the ratio of the tortuous length of flow path to the
 147 straight length of flow path (Koponen et al., 1996; Yun et al., 2006; Taiwo et al., 2016;
 148 Wu et al., 2017a). Substituting Eq. 1, the tortuosity is given by (Yu and Li, 2004):

149
$$\tau = \frac{L_t(\lambda)}{L_s} = \left(\frac{L_s}{\lambda} \right)^{D_t-1}$$

150 (11)

150
$$D_t = 1 + \frac{\ln \tau}{\ln \left(\frac{L_s}{\lambda} \right)}$$

151 (12)

151 Two kinds of 3D microstructure of granular porous media are shown in Fig. S1a–
 152 d. A regular tetrahedron and right square pyramid are selected from the 3D
 153 microstructure of granular porous media as unit cells. RTM is composed of four
 154 solid particles (Fig. S1a), and its bottom is a regular triangle (Fig. S1b), while RSPM
 155 is composed of five solid particles (Fig. S1c), and its bottom is square (Fig. S1d).
 156 For the RTM in Fig. S1a, the porosity is:

157
$$n = \frac{V_t - \frac{4}{15} \pi R_v^3}{V_t}$$

158 (13)

158 where V_t is the total volume of RTM; R_v is the median radius of solid particles. The
 159 total volume of RTM can be obtained from Eq. 13:

160
$$V_t = \frac{4\pi R_v^3}{15(1-n)} \quad (14)$$

161 Simultaneously, the volume of RTM also can be calculated by the side length
162 of RTM (L_{tl}):

163
$$V_t = \frac{\sqrt{2}}{12} L_{tl}^3 \quad (15)$$

164
$$L_{tl} = R_v \sqrt{\frac{8\sqrt{2}\pi}{5(1-n)}} \quad (16)$$

165 Consequently, the pore volume in RTM (V_{tp}) is given by:

166
$$V_{tp} = V_t - \frac{4}{15}\pi R_v^3 = \frac{4\pi R_v^3 n}{15(1-n)} \quad (17)$$

167 Approximating the irregular pore as a sphere, we can derive the diameter of the
168 sphere (λ_{t1}):

169
$$V_{tp} = \frac{4}{3}\pi \left(\frac{\lambda_{t1}}{2}\right)^3 \quad (18)$$

170
$$\lambda_{t1} = 2R_v \sqrt[3]{\frac{n}{5(1-n)}} \quad (19)$$

171 The bottom plane of RTM is a regular triangle composed of three solid particles,
172 as shown in Fig. S1b. The area of the regular triangle (A_{tb}) and the area of solid
173 particles (A_{tbs}) respectively are:

174
$$A_{tb} = \frac{\sqrt{3}}{4} L_{tl}^2 \quad (20)$$

175
$$A_{tbs} = \frac{1}{2}\pi R_v^2 \quad (21)$$

176 Then the area of pore in the bottom regular triangle (A_{tbp}) is:

177
$$A_{tbp} = \frac{\sqrt{3}}{4} L_{tl}^2 - \frac{1}{2}\pi R_v^2 \quad (22)$$

178 By approximating the irregular pore in the bottom regular triangle as a circle,
179 its diameter (λ_{t2}) can be calculated:

180
$$A_{tbp} = \pi \left(\frac{\lambda_{t2}}{2}\right)^2 \quad (23)$$

181
$$\lambda_{t2} = 2\sqrt{\frac{A_{tbp}}{\pi}} \quad (24)$$

182 In RTM, the gap length (ΔL_{tl}) between the adjacent particles is given by:

183
$$\Delta L_{tl} = L_{tl} - 2R_v = R_v \left[\sqrt[3]{\frac{8\sqrt{2}\pi}{5(1-n)}} - 2 \right] \quad (25)$$

184 The average diameter length of the capillary tubes in RTM (λ_{tl}) is quantified as:

$$185 \quad \lambda_{tl} = \frac{\lambda_{t1} + \lambda_{t2} + \Delta L_{tl}}{3} \quad (26)$$

186 Simultaneously, the side length of the regular tetrahedron in Fig. S1a is $L_{tl} =$
 187 $2R_v + \Delta L_{tl}$. Accordingly, the total volume of the regular tetrahedron in RTM
 188 microstructure is $V_t = \frac{\sqrt{2}}{12} L_{tl}^3 = \frac{\sqrt{2}}{12} (2R_v + \Delta L_{tl})^3$, and the inner pore volume is
 189 $V_{tp} = V_t - \frac{4}{15} \pi R_v^3 = \frac{\sqrt{2}}{12} (2R_v + \Delta L_{tl})^3 - \frac{4}{15} \pi R_v^3$. As a result, the porosity of RTM is
 190 expressed as:

$$191 \quad n = \frac{V_{tp}}{V_t} = \frac{\frac{\sqrt{2}}{12} (2R_v + \Delta L_{tl})^3 - \frac{4}{15} \pi R_v^3}{\frac{\sqrt{2}}{12} (2R_v + \Delta L_{tl})^3} \quad (27)$$

192 Based on Eq. (28), the ratio $p_l = \Delta L_{tl}/R_v$ can be obtained::

$$193 \quad p_l = \frac{d}{R_v} = 2 \sqrt{\frac{\sqrt{2}\pi}{5(1-n)}} - 2 \quad (28)$$

194 The tortuosity of RTM can be determined based on the ratio $p_l = \Delta L_{tl}/R_v$ of RTM and
 195 the expression of tortuosity 3D microstructure (Yun et al., 2006):

$$196 \quad \tau = \frac{\tau_1 + \tau_2}{2} \quad (29)$$

197 where $\tau_1 = 1 + \frac{\pi-2}{\frac{4\pi}{3(1-n)} + [\frac{4\pi}{3(1-n)}]^{1/3} - 2[\frac{4\pi}{3(1-n)}]^{2/3}}$, and $\tau_2 =$
 198 $\frac{6\sqrt{3p_1^2+12p_1+8} - (3p_1^2+12p_1+4)\arcsin\frac{2}{\sqrt{3(p_1+2)}} - 6(p_1+2)^2\arctg\frac{-2}{\sqrt{3p_1^2+12p_1+8}}}{8\sqrt{3}(p_1+2)}$.

199 According to the theory of the Sierpinski gasket (Fig. S2), the dimensionless
 200 pore volume of the regular tetrahedron in RTM microstructure (Fig. S1a) is given by:

$$201 \quad V_{tp} = (L_{tl}^+)^{D_f} \quad (30)$$

202 where $L_{tl}^+ = L_{tl}/d_{min}$; d_{min} is the minimum diameter of solid particles.

203 Solve Eq. (30) and the D_f can be achieved:

$$204 \quad D_f = \frac{\ln V_{tp}}{\ln L_{tl}^+} \quad (31)$$

205 The dimensionless total volume of the regular tetrahedron in RTM (V_t^+) is given
 206 by:

$$207 \quad V_t^+ = \frac{V_t}{V_{sp}} \quad (32)$$

208 where V_{sp} is the minimum volume of solid particles, $V_{sp} = \frac{4}{3} \pi (\frac{d_{min}}{2})^3 = \frac{1}{6} \pi d_{min}^3$.

209 The dimensionless total volume of the regular tetrahedron in RTM (V_t^+) can be
210 written as:

$$211 \quad V_t^+ = (L_{tl}^+)^3 V_t^+ = (L_{tl}^+)^3 \quad (33)$$

212 Afterward, L_{tl}^+ is calculated as:

$$213 \quad L_{tl}^+ = \sqrt[3]{V_t^+} = d^+ \sqrt[3]{\frac{1}{5(1-n)}} \quad (34)$$

214 where $d^+ = \frac{2R_v}{d_{min}}$. According to Yu and Cheng (2002), the value of d^+ is set as 18 or
215 24.

216 Consequently, the D_f of RTM is derived as:

$$\begin{aligned} 217 \quad D_f &= \frac{\ln V_{tp}}{\ln L_{tl}^+} = \frac{\ln(V_t^+ n)}{\ln \sqrt[3]{V_t^+}} \\ 218 \quad &= 3 + \frac{\ln(n)}{\ln(L_{tl}^+)} \\ 219 \quad &= 3 + \frac{\ln(n)}{\ln[d^+ \sqrt[3]{\frac{1}{5(1-n)}}]} \end{aligned} \quad (35)$$

220

221 For the RSPM in Fig. S1c, its porosity is given by:

$$222 \quad n = \frac{V_r - \frac{4}{9}\pi R_v^3}{V_r} \quad (36)$$

223 where V_r is the volume of RSPM. Then the volume of RSPM can be obtained from
224 Eq. 36:

$$225 \quad V_r = \frac{4\pi R_v^3}{9(1-n)} \quad (37)$$

226 Simultaneously, the volume of RTM can also be calculated by the side length
227 of RSPM (L_{rl}):

$$228 \quad V_t = \frac{\sqrt{2}}{6} L_{rl}^3 \quad (38)$$

$$229 \quad L_{rl} = R_v \sqrt[3]{\frac{8\pi}{3\sqrt{2}(1-n)}} \quad (39)$$

230 Consequently, the pore volume in RSPM is given by:

$$231 \quad V_{rp} = V_r - \frac{4}{9}\pi R_v^3 = \frac{4\pi R_v^3 n}{9(1-n)} \quad (40)$$

232 By approximating the irregular pore in RSPM as a sphere, its diameter (λ_{r1}) can

233 be calculated:

$$234 \quad V_{rp} = \frac{4}{3}\pi\left(\frac{\lambda_{rl}}{2}\right)^3 \quad (41)$$

$$235 \quad \lambda_{rl} = 2R_v^3 \sqrt[3]{\frac{n}{3(1-n)}} \quad (42)$$

236 The bottom plane of RSPM is square composed of four solid particles (Fig.
237 S1d). The area of the square (A_{rb}) and the area of solid particles (A_{rbs}) respectively are
238 expressed as:

$$239 \quad A_{rb} = L_r^2 \quad (43)$$

$$240 \quad A_{rbs} = \pi R_v^2 \quad (44)$$

241 Then, the area of pore in the bottom square of RSPM (A_{rbp}) can be obtained:

$$242 \quad A_{rbp} = L_r^2 - \pi R_v^2 \quad (45)$$

243 By approximating the irregular pore in the bottom square of RSPM as a circle,
244 its diameter (λ_{r2}) can be calculated:

$$245 \quad A_{rbp} = \pi\left(\frac{\lambda_{r2}}{2}\right)^2 \quad (46)$$

$$246 \quad \lambda_{r2} = 2\sqrt{\frac{A_{rbp}}{\pi}} \quad (47)$$

247 Moreover, the side plane of RSPM is a regular triangle composed of three solid
248 particles. Similarly, the area of the side plane of RSPM (A_{rs}) and the area of solid
249 particles (A_{rss}) respectively are expressed as:

$$250 \quad A_{rs} = \frac{\sqrt{3}}{4}L_{rl}^2 \quad (48)$$

$$251 \quad A_{rss} = \frac{1}{2}\pi R_v^2 \quad (49)$$

252 Therefore, the area of pore in the side plane of RSPM (A_{rsp}) is given by:

$$253 \quad A_{rsp} = \frac{\sqrt{3}}{4}L_{rl}^2 - \frac{1}{2}\pi R_v^2 \quad (50)$$

254 By approximating the irregular pore area in the side plane of RSPM, its diameter
255 (λ_{r3}) can be calculated:

$$256 \quad A_{rsp} = \pi\left(\frac{\lambda_{r3}}{2}\right)^2 \quad (51)$$

$$257 \quad \lambda_{r3} = 2\sqrt{\frac{A_{rsp}}{\pi}} \quad (52)$$

258 Similarly, the gap length (ΔL_{rl}) between the adjacent particles in RSPM is given
259 by:

$$260 \quad \Delta L_{rl} = L_{rl} - 2R_v = R_v \left(\sqrt[3]{\frac{8\pi}{3(1-n)}} - 2 \right) \quad (53)$$

261 The average diameter length of the capillary tube in RSPM (λ_r) is calculated as:

$$262 \quad \lambda_r = \frac{\lambda_{r1} + \lambda_{r2} + \lambda_{r3} + \Delta L_{rl}}{4} \quad (54)$$

263 Besides, the total volume of the right square pyramid in RSPM microstructure

264 is $V_r = \frac{\sqrt{2}}{6} L_{rl}^3 = \frac{\sqrt{2}}{6} (2R_v + \Delta L_{rl})^3$ and the inner pore volume is $V_{rp} = V_r - \frac{4}{9} \pi R_v^3 =$

265 $\frac{\sqrt{2}}{6} (2R_v + \Delta L_{rl})^3 - \frac{4}{9} \pi R_v^3$. Therefore, the porosity of RSPM is given by:

$$266 \quad n = \frac{V_{rp}}{V_r} = \frac{\frac{\sqrt{2}}{6} (2R_v + \Delta L_{rl})^3 - \frac{4}{9} \pi R_v^3}{\frac{\sqrt{2}}{6} (2R_v + \Delta L_{rl})^3} \quad (55)$$

267 The ratio $p_I = \Delta L_{rl} / R_v$ of RSPM is obtained by solving Eq. 56:

$$268 \quad p_1 = \frac{\Delta L_{rl}}{R_v} = 2 \sqrt[3]{\frac{\pi}{3\sqrt{2}(1-n)}} - 2 \quad (56)$$

269 Afterward, the tortuosity of RSPM can be quantified by Eq. 30). Similarly, the

270 dimensionless pore volume of the right square pyramid in RSPM microstructure (Fig.

271 S1c) is given by:

$$272 \quad V_{rp} = (L_{rl}^+)^{D_f} \quad (57)$$

273 where $L_{rl}^+ = L_{rl} / d_{min}$. D_f is achieved from Eq.58:

$$274 \quad D_f = \frac{\ln V_{rp}}{\ln L_{rl}^+} \quad (58)$$

275 The dimensionless total volume of the right square pyramid in RSPM (V_r^+) is

276 given by:

$$277 \quad V_r^+ = \frac{V_r}{V_{sp}} = \frac{V_r}{\frac{1}{6} \pi d_{min}^3} \quad (59)$$

278 Simultaneously, the dimensionless total volume of the right square pyramid in

279 RSPM (V_r^+) can be written as:

$$280 \quad V_r^+ = (L_{rl}^+)^3 \quad (60)$$

281 Afterward, L_{rl}^+ is calculated as:

$$282 \quad L_{rl}^+ = \sqrt[3]{V_r^+} = d^+ \sqrt[3]{\frac{1}{3(1-n)}} \quad (61)$$

283 Consequently, the D_f of RSPM is derived as:

$$\begin{aligned}
284 \quad D_f &= \frac{\ln V_{rp}}{\ln L_{rl}^+} = \frac{\ln(V_r^+ n)}{\ln^3 \sqrt{V_r^+}} \\
285 \quad &= 3 + \frac{\ln n}{\ln L_{rl}^+} \quad (62) \\
286 \quad &= 3 + \frac{\ln n}{\ln[d^+ \sqrt[3]{\frac{1}{3(1-n)}}]}
\end{aligned}$$

287

288 The capillary pressure of tortuous capillary tubes (P_c) can be quantified based
 289 on Yong-Laplace equation (Ahn and Seferis, 1991):

$$290 \quad P_c = \frac{\omega}{\lambda} \frac{1-n}{n} \quad (63)$$

291 where λ is the diameter of capillary tube; $\omega = F\sigma\cos\theta$; θ is the contact angle at the
 292 interface between fluid phase and solid phase; σ is the surface tension of fluid; F is
 293 the form factor related to capillary tube alignment and flow direction.

294 2.2. Sequential Gaussian simulation

295 SGS is used to generate heterogeneous porosity fields of an idealized granular
 296 aquifer to determine the effects of RTM and RSPM on DNAPL migration and
 297 remediation. Kriging is used to supply the mean and variance for conditional
 298 distributions in SGS when all distributions follow a normal distribution. SGS
 299 transforms observation data into a Gaussian distribution, after which a simple kriging
 300 estimation system is applied to simulate using the semivariogram model. Previous
 301 research suggests that 50–400 realizations are necessary to achieve a statistically stable
 302 mean realization (Eggleston et al., 1996; Hu et al., 2007). This study examines the
 303 influence of microstructure on DNAPL behavior by generating 200 porosity fields for
 304 an idealized aquifer comprised of granular porous media.

305 2.3. Numerical simulation of DNAPL migration and remediation

306 UTCHEM (University of Texas Chemical Compositional Simulator) is a
 307 multicomponent, multiphase model simulator applied to simulate the migration and

308 remediation of DNAPL in the idealized heterogeneous aquifer (Delshad et al., 1996).
309 There is no limit to the number of chemical components that can be specified by the
310 user in UTCHEM, including water, organic contaminants, surface active agents,
311 alcohols, polymers, chloride, calcium, other electrolytes, microbiological species,
312 electron acceptors, etc. Chemical reactions, dispersion, diffusion, adsorption, capillary
313 pressures, and mass transfer between phases are all included in UTCHEM. UTCHEM
314 is particularly useful for environmental applications, such as SEAR.

315 **3. Application to a synthetic heterogeneous PCE-contaminated site**

316 An idealized aquifer consists of different grades of sand, whose properties are
317 shown in Table S1 from related references. The particles of sand conform to the
318 microstructural model developed in this study. Aquifer a, as shown in Figure 1a, has a
319 rectangle area of $100 \times 51 \text{ m}^2$ and a depth of 26 m, divided into 25 (X axis) \times 17 (Y
320 axis) \times 13 (Z axis) grids, each with dimensions of $4 \times 3 \times 2 \text{ m}^3$. There are no-flow
321 boundaries at the top and bottom of the aquifer, while the left and right borders are
322 constant potential boundaries with groundwater flows from left to right (hydraulic
323 gradient is 0.005 m/m). Six injection wells and six extraction wells are installed to
324 remediate the groundwater contaminant by the SEAR technique (Fig. 1b). The SEAR
325 technique utilizes six injection wells and six extraction wells to remediate the
326 groundwater contamination. All injection and extraction wells penetrate the entire depth
327 of the aquifer.

328

329 **Fig. 1.** Idealized aquifer composed of granular porous media and boundary conditions
330 (a); set of injection and extraction wells used for contamination remediation (b).

331

332 The idealized aquifer has a porosity following a normal distribution (mean is
333 0.22, standard deviation is 0.07). The correlation length of 5 m is set for both the
334 horizontal and vertical directions of the porosity distribution. As shown in Fig. 2a,
335 one of the 200 realizations of the porosity field is generated by SGS methods in the
336 GSLIB program, and corresponding statistical analysis is performed (Fig. 2f).
337 According to Fig. 2f, the frequency distribution of the single realization follows

338 Gaussian distribution, which is the most popular distribution of variables in nature
 339 (Montgomery et al., 1987). RTM and RSPM permeability distributions are derived by
 340 Eq. 11 from the associated parameters D_t , D_f and the diameter of the capillary tube
 341 (Fig. 2b and c). The porosity field follows a normal distribution (Fig. 2f), whereas the
 342 permeability field follows a lognormal distribution (Fig. 2g and h). The phenomenon is
 343 consistent with previous findings that aquifer penetration parameters are largely
 344 characterized by lognormal distributions (Montgomery et al., 1987; Veneziano and
 345 Tabaei, 2004). Simultaneously, both RTM and RSPA exhibit some differences in their
 346 permeability fields. The mean values of individual permeability realizations of RTM
 347 and RSPM are $5.430 \times 10^{-11} \text{ m}^2$ and $2.493 \times 10^{-10} \text{ m}^2$, respectively. Furthermore, the
 348 mean values of 200 permeability realizations of RTM and RSPM are $8.360 \times 10^{-11} \text{ m}^2$
 349 and $2.643 \times 10^{-10} \text{ m}^2$, which indicates the permeability of RSPM is larger than that of
 350 RTM.

351

352 **Fig. 2.** Individual porosity field (a), permeability fields of RTM (b) and RSPM (c),
 353 entry pressure fields of RTM (d) and RSPM (e), and corresponding statistical analysis
 354 results (f–j).

355

356 According to Eqs.27 and 55 for RTM and RSPM, their median pore diameters are
 357 determined. Using Eq. 64, entry pressures for RTM and RSPM can be calculated. In
 358 detail, the individual realization of entry pressure for RTM is illustrated in Fig. 2d, and
 359 the corresponding frequency is illustrated in Fig. 2i. Simultaneously, the individual
 360 realization of entry pressure and associated frequency for RSPM is shown in Fig. 2e
 361 and j, respectively. Lognormal distributions are observed for both entry pressure
 362 distributions of RTM and RSPM. RTM and RSPM have average entry pressures of
 363 1.313 kPa and 1.449 kPa for the single realization, indicating RSPM has a slightly
 364 higher entry pressure. RTM and RSTM have no apparent difference in the frequency of
 365 entry pressure distribution (Fig. 2i and j), but RSTM and RSPM have quite different
 366 permeability frequencies(Fig. 2g and h). Therefore, microstructure has a significant
 367 impact on aquifer characteristics, which will ultimately affect associated water and
 368 contaminant transfer. The microstructure of porous media plays a significant role in

369 permeability, while entry pressure is only slightly affected.

370 As a result of a contamination spill event, the underground storage tank at the top
371 of the granular aquifer leaks PCE into the subsurface environment. To clean up PCE
372 contamination, SEAR is applied after PCE migrates freely for a long time. There are
373 four stages in the entire migration and remediation of PCE systems. Firstly, the
374 underground storage tank at the center grid block of the top layer spills 300 m^3 of PCE
375 into the aquifer every day at a rate of $10.00 \text{ m}^3/\text{day}$. The PCE spill period lasts 30 days,
376 after which the underground storage tank does not releases any PCE into the aquifer
377 during day 30 to day 100. Afterward, six injection wells are injected with 4% surface
378 active agent solution at a rate of $43.00 \text{ m}^3/\text{day}$ for $t = 100\text{--}150$ days. Simultaneously,
379 the extraction rate of six extraction wells is also $43.00 \text{ m}^3/\text{day}$. The relative permeability
380 of both oil (DNAPL) and water phases increases in the presence of surfactant, while
381 viscosity and capillary pressure are reduced by surfactant. This is a result of the
382 surfactant lowering the interfacial tension, resulting in lower residual oil saturation and
383 bound water saturation (Delshad et al., 1996; Wang et al., 2023b; Alamooti et al., 2024).
384 Therefore, surface active agents can solubilize and mobilize DNAPL in groundwater
385 systems, after which DNAPL is extracted through an extraction well from the aquifer.
386 The contaminated aquifer is then flushed with water for 150 days to sufficiently remove
387 the DNAPL. The PCE migration and remediation can be generalized to a three-
388 dimensional, unsteady, multiphase flow problem in the heterogeneous aquifer, which is
389 simulated by UTCHEM (Delshad et al., 1996) to investigate the influence of the
390 microstructure of porous media on macroscopic PCE transport and SEAR efficiency.
391 The parameters related to numerical simulation are illustrated in Fig. 2a–e and Table
392 S2.

393 **4. Results and discussion**

394 *4.1. Single realization*

395 3D visualizations of the PCE plume and 2D visualizations in the vertical section
396 plane during the entire migration and SEAR periods are shown in Fig. 3. Since PCE

397 has a greater density than groundwater, it migrates through the aquifer from the upper
 398 to the lower layers and expands the contamination plume (Fig. 3a–b). As the migration
 399 progressed, PCE plume is slightly inclined in the direction of horizontal groundwater
 400 flow (Fig. 3c). Due to heterogeneity in porosity, permeability, and entry pressure, PCE
 401 spreads irregularly in aquifers and is entrapped in zones with high permeability and
 402 low entry pressure. Therefore, residual ganglia and globules are formed in the aquifer
 403 with RTM. There is a no-flow boundary at the bottom of the aquifer, which causes
 404 PCE to accumulate at the bottom and form a large pool after long-term migration (Fig.
 405 3c).

406

407 **Fig. 3.** Simulated PCE saturation of single realization for RTM during long-term
 408 migration and remediation periods (0–300 day): PCE plumes in 3D space at $t = 10$
 409 days, 30 days, 100 days, 150 days and 300 days (a–f), respectively; corresponding
 410 PCE plume in the vertical section plane ($Y = 25.5$ m) at different times (e–j).

411

412 In comparison with the simulated results of RTM (Fig. 3a–c), the PCE transport
 413 phenomenon in aquifers with RSPM is similar (Fig. 4a–c). Nevertheless, the transport
 414 of PCE in porous media is evidently affected by the difference in microstructures.
 415 Based on the results in Fig. 2, it appears that porous media with RSPM have much
 416 higher permeability (average permeability is 2.493×10^{-10} m²) than that of RTM
 417 (average permeability is 5.430×10^{-11} m²) under the same conditions. Simultaneously,
 418 both RTM and RSTM exhibit similar frequencies of entry pressure distribution.
 419 Therefore, PCE spreads more quickly in the aquifer with RSPM due to its greater
 420 mobility. The bottom PCE pool for RSPM has a greater maximum lateral extent than
 421 that of RTM (Figs. 3f–h and 4f–h). Additionally, PCE plume in aquifers with RSPM is
 422 also inclined with a larger inclination angle along the groundwater flow direction (Figs.
 423 3 and 4).

424

425 **Fig. 4.** Simulated PCE saturation of single realization for RSPM during long-term
 426 migration and remediation periods (0–300 day): PCE plumes in 3D space at $t = 10$
 427 days, 30 days, 100 days, 150 days and 300 days (a–f), respectively; corresponding
 428 PCE plume in the vertical section plane ($Y = 25.5$ m) at different times (e–j).

429

430 After PCE migrates in groundwater over 100 days, SEAR is used to remove it.
431 Simulation results of SEAR of single realizations for RTM during $t = 100\text{--}300$ days
432 are shown in Fig. 3c–e and h–j. The remediation effect is not apparent during the first
433 $t = 100\text{--}150$ days, possibly because most PCE is in the pool state during this period
434 (Fig. 3d). Afterward, PCE remediation by SEAR is promoted by the formation of more
435 residual ganglia and globules. During the water-flooding period, the PCE volume is
436 significantly reduced, which indicates that PCE has been effectively removed from the
437 contaminated aquifer (Fig. 3e and j). A total of 236.335 m^3 PCE is removed at $t = 300$
438 days, resulting in a remediation efficiency of 78.939%.

439 Fig. 4c–e presents the simulation results of SEAR for a single realization of
440 RSPM. When $t = 150$ days, 162.3538 m^3 of PCE were removed, and remediation
441 efficiency was 54.216% (Fig. 4d). The long-term remediation resulted in the
442 removal of nearly 257.921 m^3 PCE and a remediation efficiency of 86.129%.
443 Compared to RTM, PCE is easier to clean up in aquifers with RSPM, and less PCE
444 remains in the groundwater system, resulting in a lower residual PCE volume (Fig.
445 4d–e). Simulation results show a clear correlation between microstructure and
446 macroscopic PCE remediation. It is difficult to remove PCE from the aquifer with
447 RTM using SEAR, whereas PCE can be removed more efficiently from the aquifer
448 with RSPM.

449 4.2. Numerous SGS realizations

450 RTM and RSPM simulations are also performed for 200 realizations generated
451 by the SGS method. PCE volumes in the aquifer increase linearly with time during
452 the first $t = 0\text{--}30$ days (Fig. 5a). The remaining PCE volumes after long-term SEAR
453 for RTM and RSPM are $23.305\text{--}101.434\text{ m}^3$ with a mean of 46.900 m^3 and 15.644--
454 89.411 m^3 with a mean of 32.570 m^3 , respectively. Besides, PCE infiltrates in aquifers
455 with RSPM at a faster rate along the vertical direction (Fig. 4g). Compared to the
456 residual PCE volumes in aquifers of RSPM, PCE remediation is difficult in the

457 aquifer with RTM. When surface active agents are injected into the aquifer to remove
 458 PCE from porous media at $t = 100$ days and end at $t = 150$ days, the value of ganglia-
 459 to-pool ratio (GTP) shows an obvious variation (Fig. 5b). This phenomenon indicates
 460 that surface active agent is capable of influencing GTP values of PCE plume. A
 461 decrease in GTP is followed by an increase in GTP during the water-flushing period,
 462 which suggests the architecture of the PCE plume changes during the water-flushing
 463 processes. At $t = 300$ days, GTP values are 0.183–1.365 (average value is 0.873) and
 464 0.227–1.229 (average value is 0.898) for RTM and RSPM, respectively. The
 465 relationship between cumulative PCE removal rate and remediation time is presented
 466 in Fig. 5c and the relationship between GTP value and cumulative PCE removal rate is
 467 presented in Fig. 5d.

468

469 **Fig. 5.** The change of PCE volume contained in idealized aquifer over entire migration
 470 and remediation periods (a); changes in GTP of PCE plume (b); cumulative PCE
 471 removal rate as time goes on (c); GTP value as a function of cumulative PCE removal
 472 rate (d); the center of PCE plume in horizontal axis versus time (e); vertical depth of
 473 the center of PCE plume versus time (f); second moment of PCE plume in the horizontal
 474 direction versus time (g); second moment of PCE plume versus time in vertical
 475 direction (h).

476

477 After the surface active agent injection period, there is still some PCE remaining
 478 in the aquifer. The residual PCE in groundwater is then cleaned up by following water-
 479 flushing process (Fig. 5c). At $t = 300$ days, the cumulative PCE removal volumes of
 480 RTM and RSPM reach 198.037–276.002 m^3 (mean value is 252.292 m^3) and 210.117–
 481 283.666 m^3 (mean value is 266.852 m^3), corresponding to remediation efficiency of
 482 66.129%–92.214% (mean values is 84.324%) and 70.149%–94.773% (mean value is
 483 89.122%), respectively. In comparison with RTM, SEAR has a higher remediation
 484 efficiency for aquifers with RSPM, suggesting it is easier to clean up contaminated
 485 aquifers with RSPM. Fig. 5d shows that GTP values are relatively low before 50% PCE
 486 is removed from the aquifer. After 50% of PCE is removed from the aquifer, the GTP
 487 value increases as more PCE are transformed from pool to ganglia state. After most of
 488 the PCE is cleaned up, GTP continuously increases again due to the small pool of PCE

489 remaining at the bottom of the aquifer.

490 As shown in Fig. 5e–h, the first and second moments of the PCE plume are
491 obtained through moment analysis. For RTM and RSPM, the PCE plume centers are
492 very close to each other along a horizontal direction (Fig. 5e). According to Fig. 2, the
493 permeability of porous media obtained by RSPM is higher than that of RTM. As a result,
494 the PCE plume expands more easily and contaminates the aquifer more extensively in
495 the aquifer with RSPM. Furthermore, PCE can be more easily removed from the aquifer
496 with RSPM using SEAR. During $t = 0$ –100 days (migration period), PCE plumes in
497 aquifers with RSPM have a smaller second moment in the horizontal direction than that
498 in aquifers with RTM, which may be caused by the larger transport capacity of PCE in
499 the aquifer with RSPM. During $t = 100$ –300 days (SEAR period), the remediation
500 efficiency obtained by RSPM is higher than that obtained by RTM because PCE is
501 easier to remove in the aquifer with RSPM. Consequently, the second moments along
502 the horizontal direction for RTM and RSPM are 10.896–145.660 m² (mean value is
503 51.825 m²) and 17.598–108.000 m² (mean value is 49.195 m²) at $t = 300$ days, which
504 indicates RTM has slightly larger values of the second moments along the horizontal
505 direction (Fig. 5g). At $t = 300$ days, PCE plume centers are similar along the vertical
506 direction for RTM and RSPM, while the plume extent obtained by RTM is larger than
507 that obtained by RSPM (Fig. 5f). What's more, second moments along vertical direction
508 for 200 realizations of RTM and RSPM are 18.837–153.170 m² (mean value is 65.766
509 m²) and 27.344–133.040 m² (mean value is 69.529 m²), respectively (Fig. 5h).
510 Combining the second moments along horizontal and vertical directions, PCE plume
511 area in aquifer with RSPM is larger than that of RTM, implying RSPM can cause a
512 wider contamination plume.

513 Significantly, PCE is a typical DNAPL contaminant with a larger density
514 compared with water, so the conclusions of this study are applicable to other similar
515 DNAPL contaminants. However, other pollutants, such as light non-aqueous phase
516 liquid (LNAPL) contaminants, have smaller densities compared with DNAPL and
517 water. If other LNAPL contaminants are selected, the migration and remediation
518 will be changed. The effects of 3D microstructure on the transport and remediation

519 of other different contaminants in heterogeneous porous media are beyond this study
520 and will be explored in our future research.

521 **5. Conclusions**

522 To investigate the influence of the microstructure of granular porous media on
523 macroscopic contaminant migration and remediation, the fractal models are
524 developed to quantify the macroscopic parameters (such as porosity, permeability,
525 and entry pressure) for two 3D microstructures of porous media-RTM and RSPM.
526 Using the SGS method, 200 realizations of an idealized aquifer composed of different
527 grades of sand are generated. The long-term PCE transport and SEAR process is
528 simulated by UTCHEM using distributions of porosity, permeability, and entry
529 pressure derived from the fractal models of RTM and RSPM. Results suggest the
530 mobility of PCE plume in aquifers with RTM is less than that in aquifers with RSPM.
531 Simultaneously, PCE contamination is difficult to remove from aquifers with RTM by
532 SEAR. After long-time SEAR remediation, the cumulative PCE removal rates are
533 66.129%–92.214% (mean value is 84.324%) for 200 realizations of RTM, and
534 70.149%–94.773% (mean value is 89.122%) for 200 realizations of RSPM,
535 respectively. Moreover, The GTP of the PCE plume obtained by RSPM is mostly higher
536 than that obtained by RTM. Findings from this work suggest that the microstructure of
537 granular porous media is fundamental to understanding aquifer characteristics and
538 contaminant migration as well as remediation effects. Furthermore, the migration
539 behavior of DNAPL and other organic pollutants (such as chlorobenzene, light non-
540 aqueous phase liquid) in groundwater under different conditions (simulation factors
541 are permeability coefficient and pressure), DNAPL remediation by other materials
542 (such as oxidation agents and adsorption agents), and verification of 3D microstructure
543 models of porous media by experiments and actual site research will be explored in our
544 future research to provide recommendations for prediction and management of PCE
545 migration.

546

547 **CRedit authorship contribution statement**

548 Z. C.: conceptualization, methodology, writing–original draft, project administration;

549 M.W.: conceptualization, methodology, writing–original draft, writing-review &

550 editing, funding acquisition, project administration; Y.R.H., C.H.M., Q.S.L., J.F.W.,

551 J.C.W., B.X.H., G.P.L.: conceptualization, methodology.

552 **Declaration of competing interests**

553 The authors declare that they have no known competing financial interests or personal

554 relationships that could have appeared to influence the work reported in this paper.

555 **Acknowledgments**

556 This research was supported by the National Key Research and Development Plan

557 of China (no. 2019YFC1804302), the Natural Science Foundation of Guangdong

558 Province (no. 2023A1515012228) and Guangdong Provincial Environmental

559 Protection Fund (Guangdong Financial Budget (2024) 4).

560 **References**

561 Alamooti, A., Colombano, S., Shoker, A., Ahmadi-Sénichault, A., Lion, F., Cazaux, D.,

562 et al., 2024. Enhancing remediation of residual DNAPL in multilayer aquifers:

563 Post-injection of alcohol-surfactant-polymer mixtures. *Sci. Total Environ.* 918,

564 170680.

565 Asuquo, J.E., Etim, E.E., 2012. Physicochemical and bacteriological studies of selected

566 borehole water in Uyo Metropolis in Akwa Ibom State. *Int. J. Mod. Chem.*

567 2(1),7-14.

568 Bakshevskaya, V.A., Pozdniakov, S.P., 2016. Simulation of hydraulic heterogeneity and

569 upscaling permeability and dispersivity in Sandy-Clay formations. *Math*570 *Geosci* 48, 45-64.571 Bear, J., 1972. *Dynamics of fluids in porous media*. Dover, New York.

572 Bian, J.M., Ruan, D.M., Wang, Y., Sun, X.Q., Gu, Z.Q., 2023. Bayesian ensemble

- 573 machine learning-assisted deterministic and stochastic groundwater DNAPL
574 source inversion with a homotopy-based progressive search mechanism. *J.*
575 *Hydrol.* 624, 129925.
- 576 Bob, M.M., Brooks, M.C., Mravik, S.C., Wood, A.L., 2008. A modified light
577 transmission visualization method for DNAPL saturation measurements in 2-
578 D models. *Adv. Water Resour.* 31, 727-742.
- 579 Boswinkel, J.A., 2000. Information Note. International Groundwater Resources
580 Assessment Centre (IGRAC), Netherland Institute of Applied Geoscience,
581 Netherlands.
- 582 Bradford, S.A., Vendlinski, R.A., Abriola, L.M., 1999. The entrapment and long-term
583 dissolution of tetrachloroethylene in fractional wettability porous media. *Water*
584 *Resour. Res.* 35(10), 295-2964.
- 585 Cai, J.C., Yu, B.M., Zou, M.Q., M, M.F., 2010. Fractal analysis of invasion depth of
586 extraneous fluids in porous media. *Chem. Eng. Sci.* 65, 5178-5186.
- 587 Chen, L.F., Ding, G.T., Lu, J., Liu, Y.X., Wei, S.M., Guo, X.J., et al., 2024. Gas tube
588 effect: A transport mode of deeply buried volatile DNAPLs to shallow strata. *J.*
589 *Hydrol.* 630, 130696.
- 590 Cochenec, M., Davarzani, H., Davit, Y., Colombano, S., Ignatiadis, I., Masselot, G.,
591 et al., 2022. Impact of gravity and inertia on stable displacements of DNAPL
592 in highly permeable porous media. *Adv. Water Resour.* 162, 104139.
- 593 Cui, Q.L., Wu, H.N., Shen, S.L., Yin, Z.Y., Horpibulsuk, S., 2016. Protection of
594 neighbour buildings due to construction of shield tunnel in mixed ground with
595 sand over weathered granite. *Environ. Earth Sci.* 75, 458.
- 596 C.Carroll, K., McDonald, K., Marble, J., Russo, A.E., Brusseau, M.L., 2015. The
597 impact of transitions between two-fluid and three-fluid phases on fluid
598 configuration and fluid-fluid interfacial area in porous media. *Water Resour.*
599 *Res.* 51, 7189-7201.
- 600 Delshad, M., Pope, G.A., Sepehrnoori, K., 1996. A compositional simulator for
601 modeling surfactant enhanced aquifer remediation, 1 Formation. *J. Contam.*
602 *Hydrol.* 23, 303-327.
- 603 Demiray, Z., Akyol, N.H., Akyol, G., Coptly, N.K., 2023. Surfactant-enhanced in-situ
604 oxidation of DNAPL source zone: Experiments and numerical modeling. *J.*
605 *Contam. Hydrol.* 258, 104233.
- 606 Eggleston, J.R., Rojstaczer, S.A., Peirce, J.J., 1996. Identification of hydraulic

- 607 conductivity structure in sand and gravel aquifers: Cape Cod data set. *Water*
608 *Resour. Res.* 32, 1209–1222.
- 609 Essaid, H.I., Bekins, B.A., Cozzarelli, I.M., 2015. Organic contaminant transport and
610 fate in the subsurface: Evolution of knowledge and understanding. *Water*
611 *Resour. Res.* 51, 4861-4902.
- 612 Feng, Y.J., Yu, B.M., 2007. Fractal dimension for tortuous streamtubes in porous media.
613 *Fractals* 15, 385-390.
- 614 Guo, S.J., Zha, Y.Y., Zhong, H., Wang, X., Xu, D., 2023. Numerical investigations of
615 influence on thermal conductive heating in DNAPL-impacted soils by
616 heterogeneity. *J. Hydrol.* 258, 104232.
- 617 Herraiz-Carboné, M., Santos, A., Checa-Fernández, A., Domínguez, C.M., Cotillas, S.,
618 2024. Removal of organochlorine pollutants from DNAPL-saturated
619 groundwater using electrolysis with MMO anodes. *Chem. Eng. J.* 486, 150238.
- 620 Hou, Z.Y., Zhao, K., Wang, S., Wang, Y., Lu, W.X., 2024. Bayesian hybrid-kernel
621 machine-learning-assisted sensitivity analysis and sensitivity-relevant inverse
622 modeling for groundwater DNAPL contamination. *J. Hydrol.* 633, 131009.
- 623 Hu, K., White, R., Chen, D., Li, B., Li, W., 2007. Stochastic simulation of water
624 drainage at the field scale and its application to irrigation management. *Agr.*
625 *Water Manage.* 89, 123-130.
- 626 Huang, J.Q., Christ, J.A., Goltz, M.N., Demond, A.H., 2015. Modeling NAPL
627 dissolution from pendular rings in idealized porous media. *Water Resour. Res.*
628 51, 8182-8197.
- 629 Jeong, E., Kim, Y.I., Lee, J.Y., Raza, M., 2023. Microplastic contamination in
630 groundwater of rural area, eastern part of Korea. *Sci. Total Environ.* 895,
631 165006.
- 632 Kang, X.Y., Power, C., Kokkinaki, A., Revil, A., Wu, J.C., Shi, X.Q., et al., 2023.
633 Characterization of DNAPL source zones in clay-sand media via joint
634 inversion of DC resistivity, induced polarization and borehole data. *J. Contam.*
635 *Hydrol.* 258, 104240.
- 636 Katz, A.J., Thompson, A.H., 1985. Fractal sandstone: Implications for conductivity and
637 pore formation. *Phys. Rev. Lett.* 54, 325-332.
- 638 Kim, T., Han, W.S., Yoon, S., Kang, P.K., Shin, J.Y., Nam, M.J., 2024. Evaluation of
639 the impact of transition from porous to fractured rock media on 3D field-scale

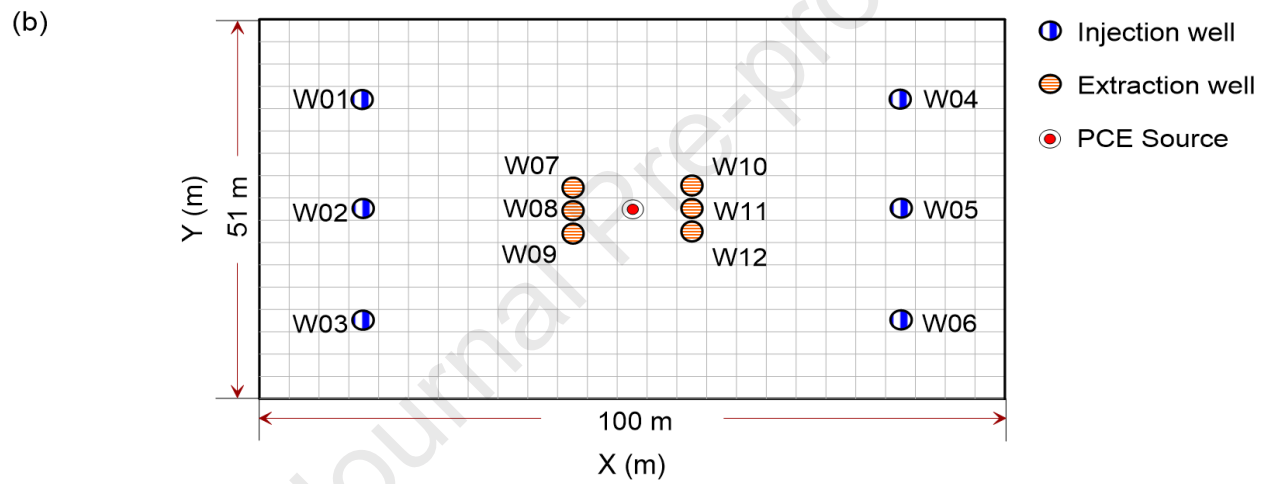
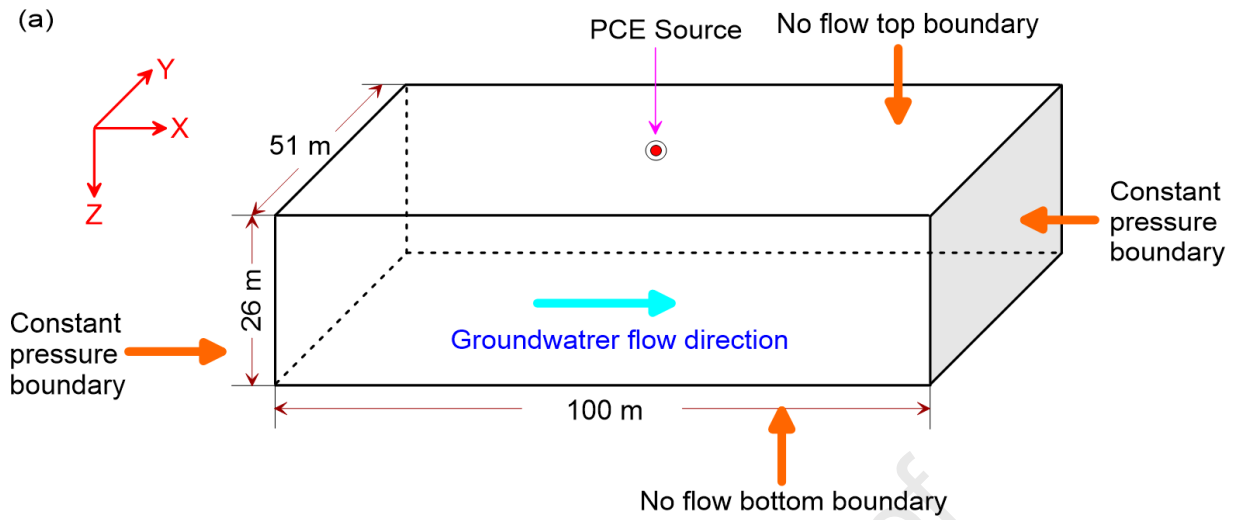
- 640 DNAPLs contamination. *J. Hazard. Mater.* 462, 132711.
- 641 Koponen, A., Kataja, M., Timonen, J., 1996. Tortuous Flow in Porous Media. *Phys. Rev.*
642 *E* 54, 406-410.
- 643 Krohn, C.E., 1988. Sandstone fractal and Euclidean pore volume distributions. *J.*
644 *Geophys. Res.* 93, 3286-3296.
- 645 Kuang, X.X., Liu, J.G., Scanlon, B.R., Jiao, J.J., Jasechko, S., Lancia, M., et al., 2024.
646 The changing nature of groundwater in the global water cycle. *Science*
647 383(6686), eadf0630.
- 648 Landrigan, P., Fuller, R., Acosta, N.J.R., Adeyi, O., Arnold, R., Basu, N., et al., 2018.
649 The Lancet Commission on pollution and health. *Lancet* 391,462-512.
- 650 Li, L., Yu, B.M., 2013. Fractal analysis of the effective thermal conductivity of
651 biological media embedded with randomly distributed vascular trees. *Int. J.*
652 *Heat Mass Tran.* 67, 74-80.
- 653 Liang, C., Hsieh, C.L., 2015. Evaluation of surfactant flushing for remediating EDC-
654 tar contamination. *J. Contam. Hydrol.* 177-178, 158-166.
- 655 Liang, C., Lai, M.C., 2008. Trichloroethylene degradation by zero valent iron activated
656 persulfate oxidation. *Environ. Eng. Sci.* 25(7), 1071-1077.
- 657 Liu, H., Li, Y.X., He, X., Sissou, Z., Tong, L., Yarnes, C., et al., 2016. Compound-
658 specific carbon isotopic fractionation during transport of phthalate esters in
659 sandy aquifer. *Chemosphere* 144, 1831-1836.
- 660 Liu, L., 2005. Modeling for surfactant-enhanced groundwater remediation processes at
661 DNAPLs-contaminated sites. *J. Environ. Inform.* 5(2), 42-52.
- 662 Liu, Y., Wang, S., McDonough, C.A., Khairy, M., Muir, D.C.G., Helm, P.A., et al., 2016.
663 Gaseous and freely-dissolved PCBs in the lower great lake based on passive
664 sampling: spatial trends and air-water exchange. *Environ. Sci. Technol.* 50,
665 4932-4939.
- 666 Montgomery, R.H., Loftis, J.C., Harris, J., 1987. Statistical characteristics of ground-
667 water quality variables. *Ground Water* 25(2), 176-184.
- 668 Omirbekov, S., Colombano, S., Alamooti, A., Batikh, A., Cochenec, M., Amanbek, Y.,
669 et al., 2023. Experimental study of DNAPL displacement by a new densified
670 polymer solution and upscaling problems of aqueous polymer flow in porous
671 media. *J. Contam. Hydrol.* 252, 104120.
- 672 O'Carroll, D.M., Bradford, S.A., Abriola, L.M., 2004. Infiltration of PCE in a system
673 containing spatial wettability variations. *J. Contam. Hydrol.* 73, 39-63.

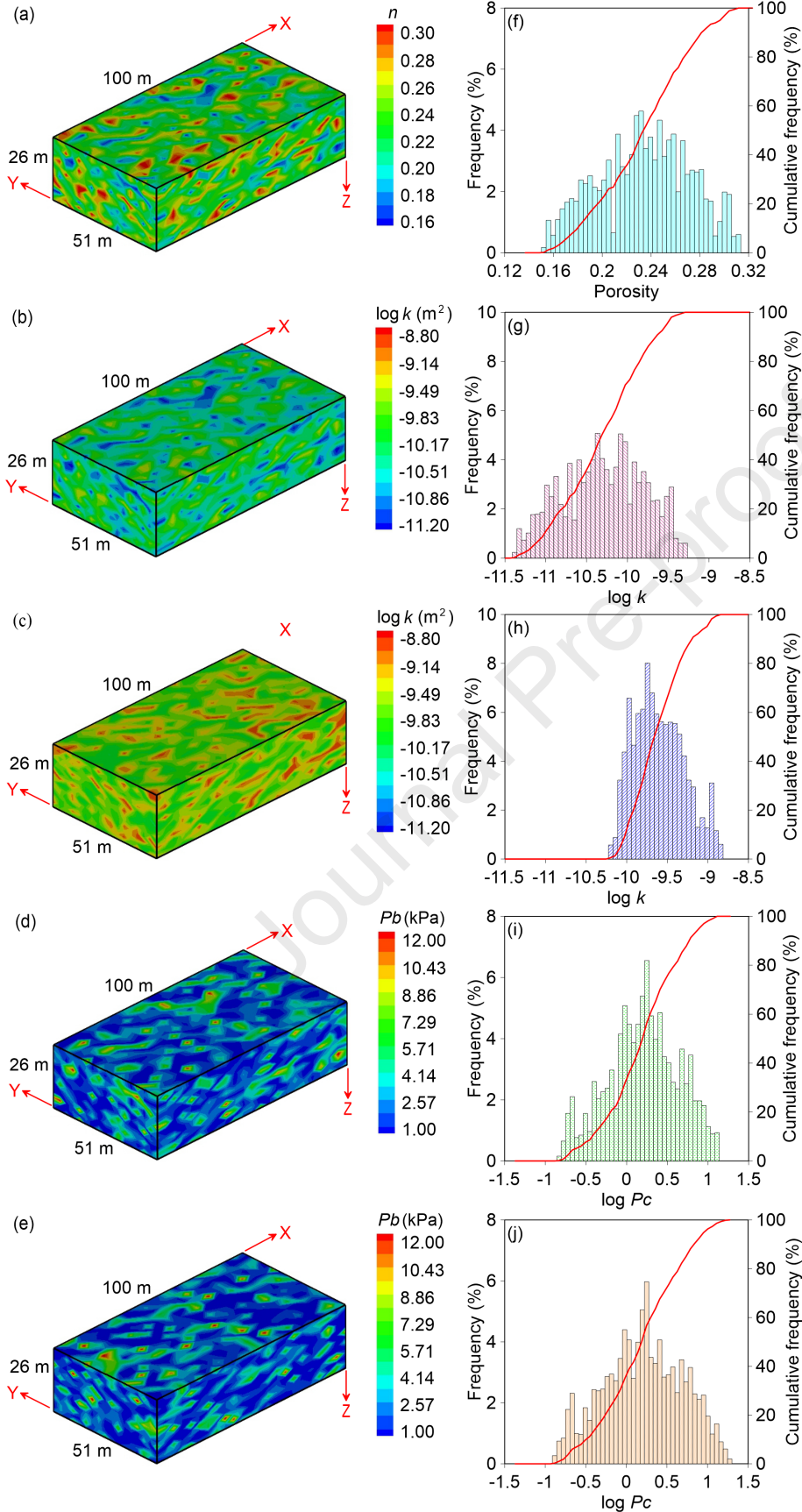
- 674 Pfeifer, P., Avnir, D., 1983. Chemistry in Nonintegral dimensions between two and three.
675 I. Fractal theory of heterogeneous surface. *J. Chem. Phys.* 79, 3558-3565.
- 676 Schaefer, C.E., White, E.B., Lavorgna, G.M., Annable, M.D., 2016. Dense nonaqueous-
677 phase liquid architecture in fractured bedrock: implications for treatment and
678 plume longevity. *Environ. Sci. Technol.* 50, 207-213.
- 679 Shen, Y.Q., Xu, P., Qiu, S.X., Rao, B.Q., Yu, B.M., 2020. A generalized thermal
680 conductivity model for unsaturated porous media with fractal geometry. *Int. J.*
681 *Heat Mass Tran.* 152, 119540.
- 682 Shi, J.X., Chen, X.H., Ye, B., Wang, Z.W., Sun, Y.Y., Wu, J.C., et al., 2023. A
683 comparative study of DNAPL migration and transformation in confined and
684 unconfined groundwater systems. *Water Res.* 245, 120649.
- 685 Taiwo, O.O., Finegan, D.P., Eastwood, D.S., Fife, J.L., Brown, L.D., Darr, J.A., et al.,
686 2016. Comparison of three-dimensional analysis and stereological techniques
687 for quantifying lithium-ion battery electrode microstructures. *J. Microsc.*
688 263(3), 280-292.
- 689 Valipour, M., 2012. Comparison of surface irrigation simulation models: Full
690 hydrodynamic, zero inertia, kinematic wave. *J. Agr. Sci.* 4(12), 68-74.
- 691 Valipour, M., 2015. Future of agricultural water management in Africa. *Arch. Agron.*
692 *Soil Sci.* 61(7), 907-927.
- 693 Valipour, M., Singh, V.P., 2016. Global experiences on wastewater irrigation:
694 challenges and Prospects, in: Maheshwari, B., Singh, V.P., Thoradeniya, B.,
695 Balanced urban development: options and strategies for liveable cities. Volume
696 72 of the series Water Science and Technology Library, 2016, pp. 289-327.
- 697 Veneziano, D., Tabaei, A., 2004. Nonlinear spectral analysis of flow through porous
698 media with isotropic lognormal hydraulic conductivity. *J. Hydrol.* 294, 4-17.
- 699 Wang, Y., Bian, J., Sun, X., Ruan, D., Gu, Z., 2023a. Sensitivity-dependent dynamic
700 searching approach coupling multi-intelligent surrogates in homotopy
701 mechanism for groundwater DNAPL-source inversion. *J. Contam. Hydrol.* 255,
702 104151.
- 703 Wang, Z.J., Yang, Z.B., Hu, R., Chen, Y.F., 2023b. Mass transfer during surfactant-
704 enhanced DNAPL remediation: Pore-scale experiments and new correlation. *J.*
705 *Hydrol.* 621, 129586.
- 706 Weathers, T.S., Harding-Marjanovic, K., Higgins, C.P., Alvarez-Cohen, L., Sharp, J.O.,
707 2016. Perfluoroalkyl acids inhibit reductive dechlorination of Trichloroethene

- 708 by repressing dehalococcoides. *Environ. Sci. Technol.* 50, 240-248.
- 709 Wu, M., Cheng, Z., Lu, G.P., Mo, C.H., Hao, Y.R., Li, Q.S., et al., 2023. Impact of
710 grain geometry on chlorohydrocarbon contaminant transformation and
711 reductive dichlorination activity. *J. Petrol. Sci. Eng.* 229, 212143.
- 712 Wu, M., Cheng, Z., Wu, J.F., Wu, J.C., 2017a. Quantifying representative elementary
713 volume of connectivity for translucent granular materials by light transmission
714 micro-tomography. *J. Hydrol.* 545, 12-27.
- 715 Wu, M., Wu, J.F., Wu, J.C., 2017b. Simulation of DNAPL migration in heterogeneous
716 translucent porous media based on estimation of representative elementary
717 volume. *J. Hydrol.* 553, 276-288.
- 718 Wu, M., Wu, J.F., Wu, J.C., Hu, B.X., 2018. Effects of microarrangement of solid
719 particles on PCE migration and its remediation in porous media. *Hydrol. Earth
720 Syst. Sci.* 22(2), 1001-1015.
- 721 Wu, M., Wu, J.F., Wu, J.C., Hu, B.X., 2020. A new criterion for determining the
722 representative elementary volume of translucent porous media and inner
723 contaminant. *Hydrol. Earth Syst. Sci.* 24(12), 5903-5917.
- 724 Yang, C.G., Zhang, C.P., Liu, F.Y., Dong, J., 2024. Remediation of DNAPL-
725 contaminated heterogeneous aquifers using colloidal biliquid aphron:
726 Multiscale experiments and pore-scale simulations. *J. Hydrol.* 628, 130532.
- 727 Yang, S.S., Cui, R.K., Yuang, X.B., Zou, M.Q., 2023. Fractal study on permeability
728 characteristics in rough and dense porous media. *Chem. Eng. Sci.* 282, 119265.
- 729 Yang, X., Du, Y.P., Xu, Q., Wu, F.T., Zhou, T., Zhao, C.Y., 2022. Pores integrated
730 fractal (PIF) analysis on transportation in porous media considering spatial
731 distribution of pores and genuine tortuosity. *Int. J. Heat Mass Tran.* 187,
732 122528.
- 733 Yannopoulos, S.I., Lyberatos, G., Theodossiou, N., Li, W., Valipour, M., Tamburrino,
734 A., et al., 2015. Evolution of water lifting devices (pumps) over the centuries
735 worldwide. *Water* 7, 5031-5060.
- 736 Yu, B.M., 2005. Fractal character for tortuous streamtubes in porous media. *CHIN.
737 PHYS. LETT.* 22, 158-160.
- 738 Yu, B.M., Cai, J.C., Zou, M.Q., 2009. On the physical properties of apparent two-phase
739 fractal porous media. *Vadose Zone J.* 8, 177-186.
- 740 Yu, B.M., Cheng, P., 2002. Fractal models for the effective thermal conductivity of
741 bidispersed porous media. *J. Thermophys. Heat Tr.* 16, 22-29.

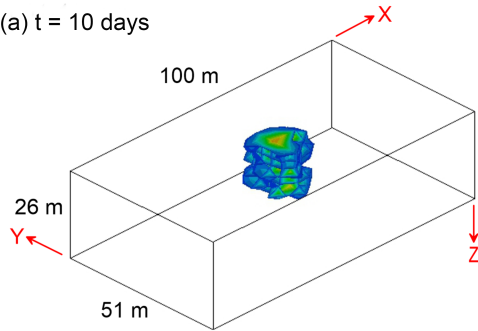
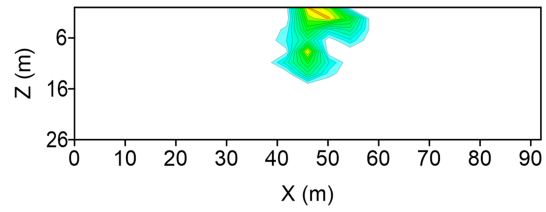
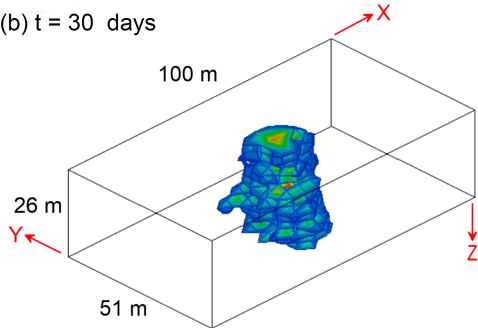
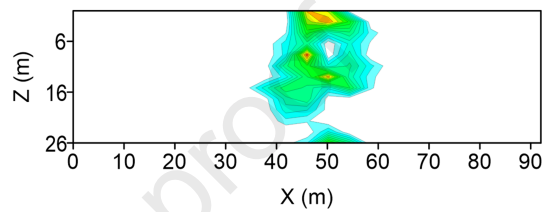
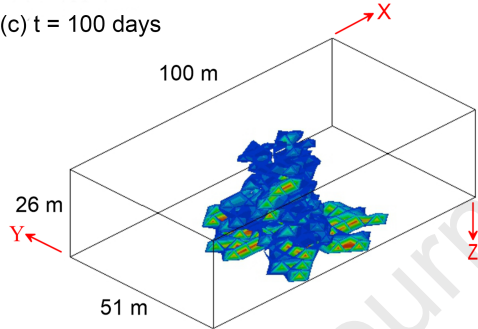
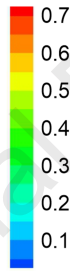
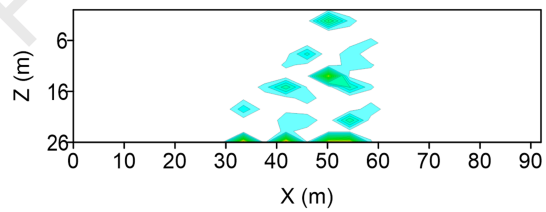
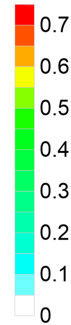
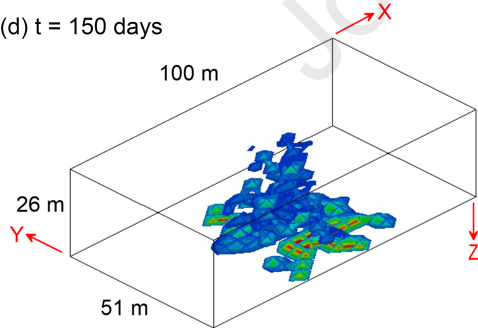
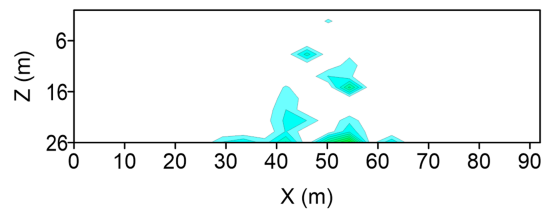
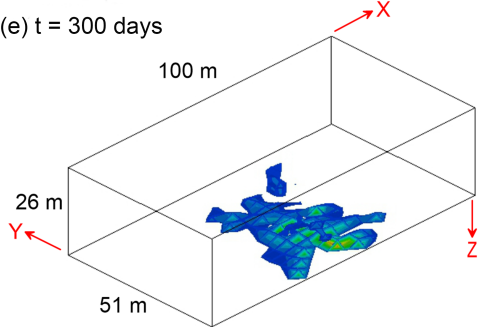
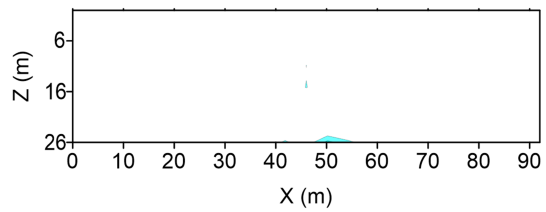
- 742 Yu, B.M., Li, J.H., 2004. A geometry model for tortuosity of flow path in porous media.
743 CHIN. Phys. Lett. 21, 1569-1571.
- 744 Yun, M.J., Yu, B.M., Xu, P., Wu, J.S., 2006. Geometrical models for tortuosity of
745 streamlines in three-dimensional porous media. Can. J. Chem. Eng. 84, 301-
746 309.
- 747 Zhang, S., Mao, G.Z., Crittenden, J., Liu, X., Du, H.B., 2017. Groundwater remediation
748 from the past to the future: A bibliometric analysis. Water Res. 119, 114-125.
- 749
- 750

Journal Pre-proof



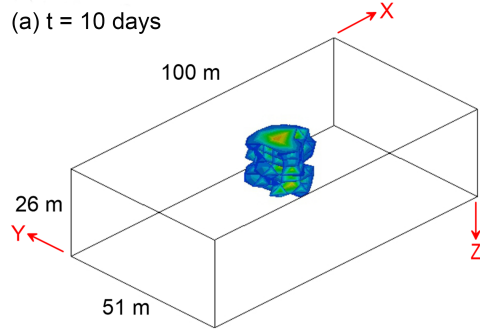


Journal Pre-proof

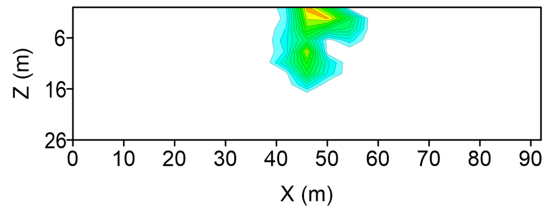
(a) $t = 10$ days(f) $t = 10$ days, $Y = 25.5$ m(b) $t = 30$ days(g) $t = 30$ days, $Y = 25.5$ m(c) $t = 100$ days S_{PCE} (h) $t = 100$ days, $Y = 25.5$ m S_{PCE} (d) $t = 150$ days(i) $t = 150$ days, $Y = 25.5$ m(e) $t = 300$ days(j) $t = 300$ days, $Y = 25.5$ m

Journal Pre-proof

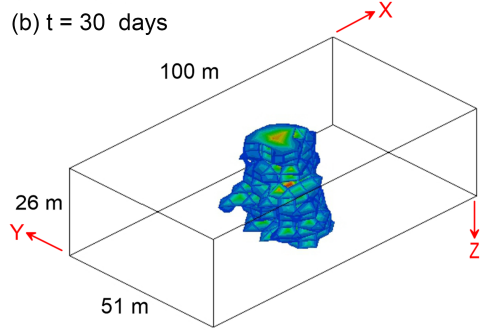
(a) $t = 10$ days



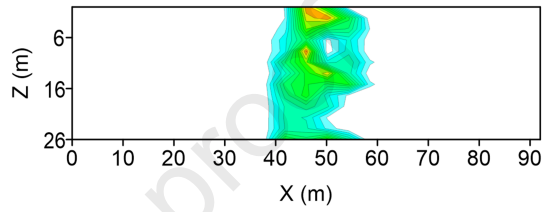
(f) $t = 10$ days, $Y = 25.5$ m



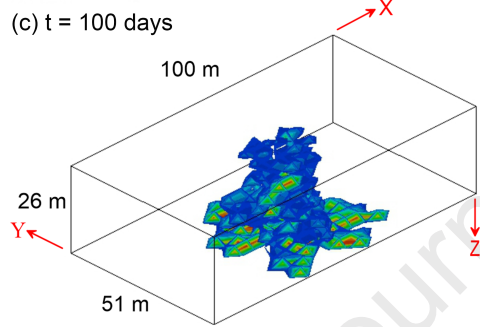
(b) $t = 30$ days



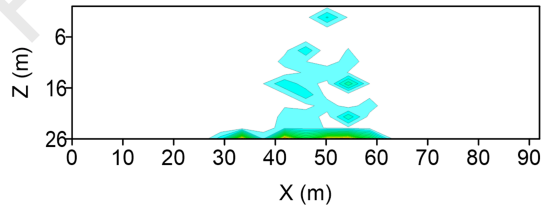
(g) $t = 30$ days, $Y = 25.5$ m



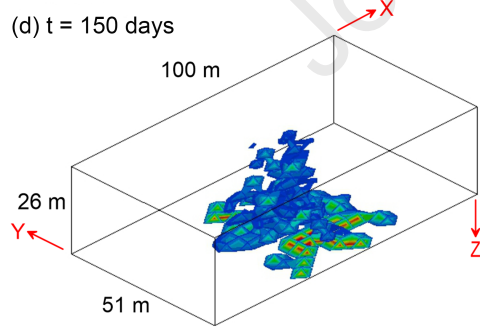
(c) $t = 100$ days



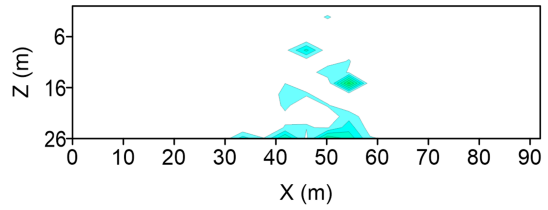
(h) $t = 100$ days, $Y = 25.5$ m



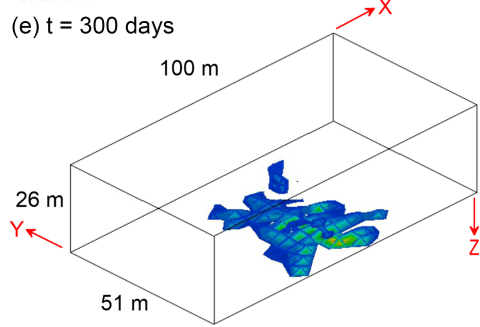
(d) $t = 150$ days



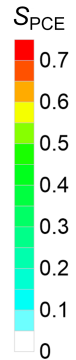
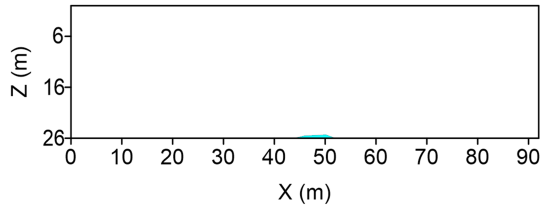
(i) $t = 150$ days, $Y = 25.5$ m



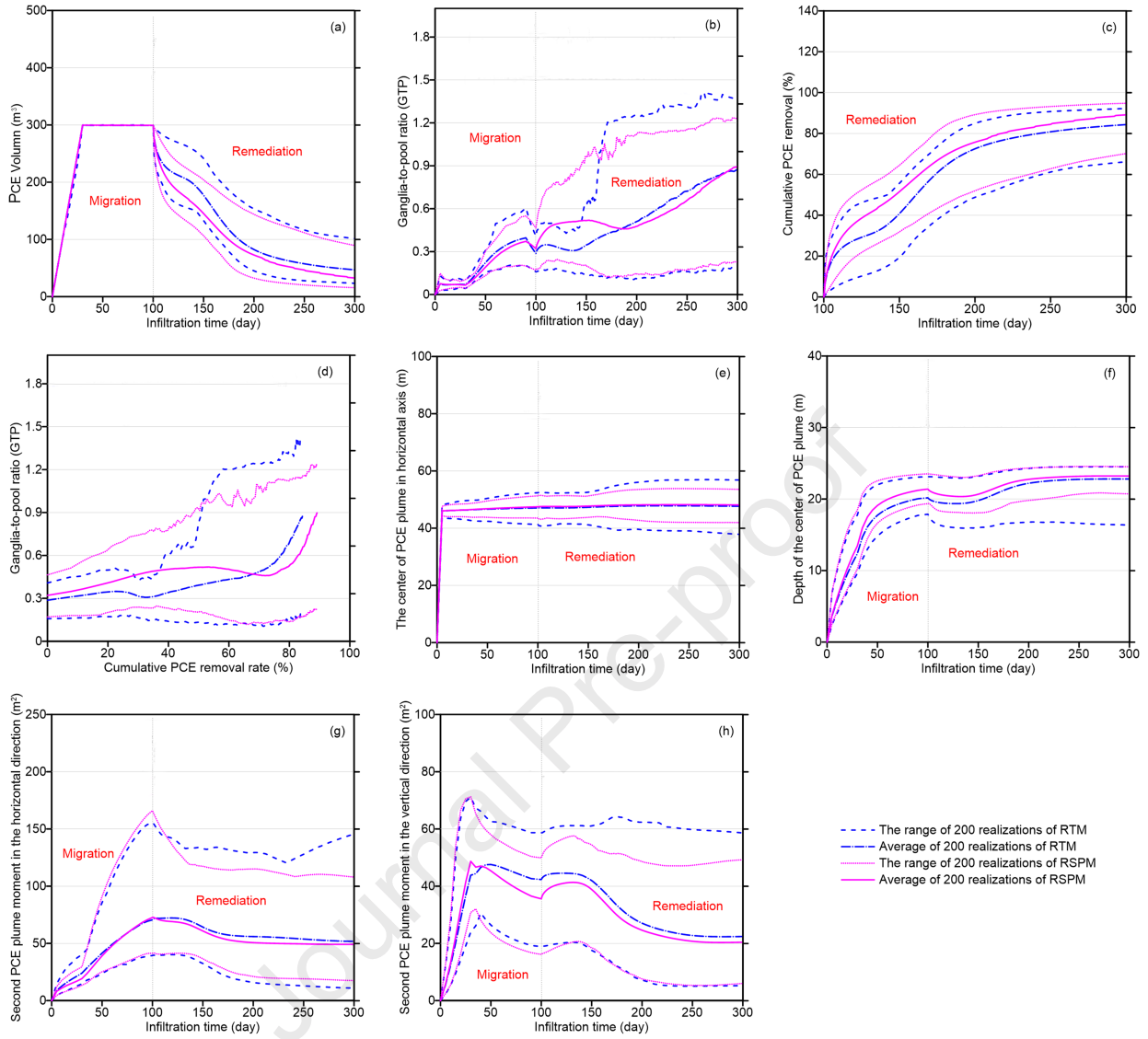
(e) $t = 300$ days

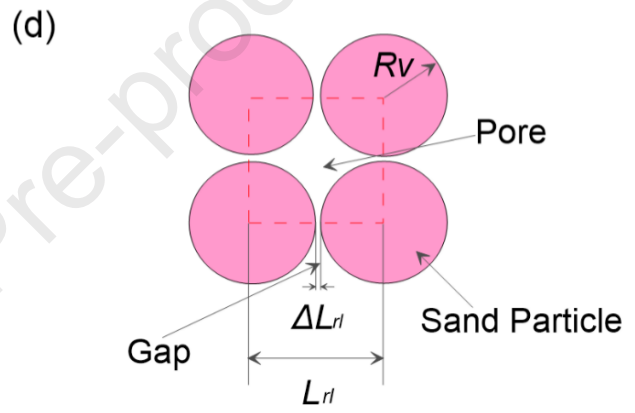
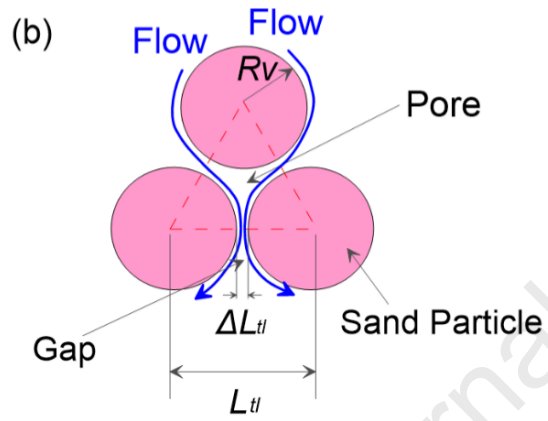
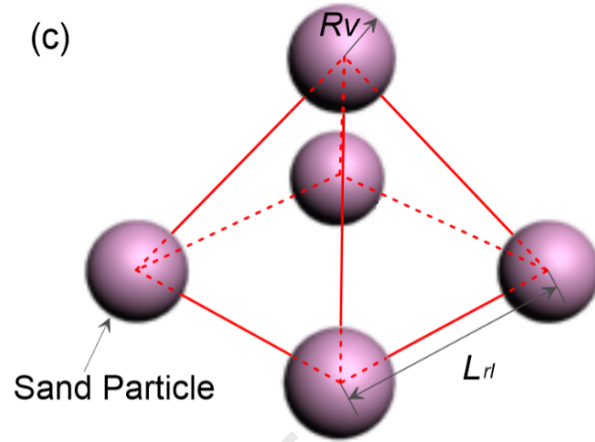
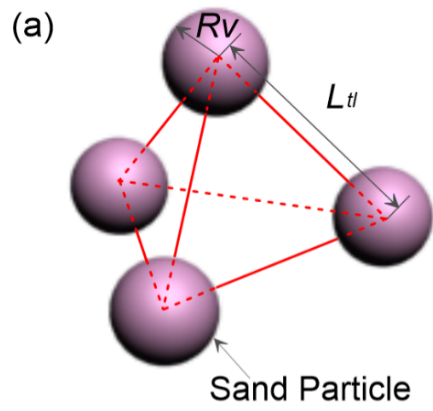


(j) $t = 300$ days, $Y = 25.5$ m



Journal Pre-proof





Highlights

- Fractal models are developed for RTM and RSPM.
- Lognormal distributions of permeability and entry pressure conform to previous study.
- DNAPL infiltrates more quickly in granular aquifer of RSPM than RTM.
- RSPM can cause a larger DNAPL plume than RTM.
- DNAPL contamination is harder to remove by SEAR in granular aquifer of RTM than RSPM.